AMERICAN SOCIETY FOR MICROBIOLOGY | Journal of Virology

Virology | Full-Length Text

Identification of a short sequence motif in the influenza A virus pathogenicity factor PB1-F2 required for inhibition of human NLRP3

Filo Silva,[1] Inês Boal-Carvalho,[1] Nathalia Williams,[1] Mehdi Chabert,[1] Chengyue Niu,[1] Dalila Hedhili,[1] Hélèna Choltus,[1] Nicolas Liaudet,[2] Nadia Gaïa,[3] Wolfram Karenovics,[4] Patrice Francois,[1,4] Mirco Schmolke[1,5]

AUTHOR AFFILIATIONS See affiliation list on p. 14.

ABSTRACT Influenza A virus infection activates the NLRP3 inflammasome, a multiprotein signaling complex responsible for the proteolytic activation and release of the proinflammatory cytokine IL-1β from monocytes and macrophages. Some influenza A virus (IAV) strains encode a short 90-amino acid peptide (PB1-F2) on an alternative open reading frame of segment 2, with immunomodulatory activity. We recently demonstrated that contemporary IAV PB1-F2 inhibits the activation of NLRP3, potentially by NEK7-dependent activation. PB1-F2 binds to NLRP3 with its C-terminal 50 amino acids, but the exact binding motif was unknown. On the NLRP3 side, the interface is formed through the leucine-rich-repeat (LRR) domain, potentially in conjunction with the pyrin domain. Here, we took advantage of PB1-F2 sequences from IAV strains with either weak or strong NLRP3 interaction. Sequence comparison and structure prediction using Alphafold2 identified a short four amino acid sequence motif (TQGS) in PB1-F2 that defines NLRP3-LRR binding. Conversion of this motif to that of the non-binding PB1-F2 suffices to lose inhibition of NLRP3 dependent IL-1β release. The TQGS motif further alters the subcellular localization of PB1-F2 and its colocalization with NLRP3 LRR and pyrin domain. Structural predictions suggest the establishment of additional hydrogen bonds between the C-terminus of PB1-F2 and the LRR domain of NLRP3, with two hydrogen bonds connecting to threonine and glutamine of the TQGS motif. Phylogenetic data show that the identified NLRP3 interaction motif in PB1-F2 is widely conserved among recent IAV-infecting humans. Our data explain at a molecular level the specificity of NLRP3 inhibition by influenza A virus.

IMPORTANCE Influenza A virus infection is accompanied by a strong inflammatory response and high fever. The human immune system facilitates the swift clearance of the virus with this response. An essential signal protein in the proinflammatory host response is IL-1b. It is released from inflammatory macrophages, and its production and secretion depend on the function of NLRP3. We had previously shown that influenza A virus blocks NLRP3 activation by the expression of a viral inhibitor, PB1-F2. Here, we demonstrate how this short peptide binds to NLRP3 and provide evidence that a four amino acid stretch in PB1-F2 is necessary and sufficient to mediate this binding. Our data identify a new virus-host interface required to block one signaling path of the innate host response against influenza A virus.

KEYWORDS influenza, NLRP3, PB1-F2, inflammasome, IL-1beta, inflammation, macrophage, protein interactions

Influenza A viruses (IAV) infect the respiratory tract of humans and provoke a robust proinflammatory response, which contributes substantially to the experienced clinical

Editor Anice C. Lowen, Emory University School of Medicine, Atlanta, Georgia, USA

Address correspondence to Mirco Schmolke, mirco.schmolke@unige.ch.

Nathalia Williams and Mehdi Chabert contributed equally to this article.

The authors declare no conflict of interest.

See the funding table on p. 15.

Received 4 March 2024
Accepted 14 March 2024
Published 3 April 2024

symptoms (1). A key cytokine in this context is IL-1β (2). It is produced mostly by monocytic cells as pro-IL-1β and processed proteolytically upon stimulation of cells into its active form (3). Secreted IL-1β is required to respond appropriately to inflammatory stimuli, and consequently, IL-1β-deficient mice do not develop fever when, e.g., injected with turpentine (4). In the context of IAV infection, IL-1β signaling is crucial for the accompanying immunopathology (5) and for inducing T-cell immunity against mucosal vaccination against IAV (6). Diverse approaches were described to limit IAV-induced immunopathology by inhibiting NLRP3 activation (7–9).

On a cellular level, stimulation of the NLRP3 inflammasome and activation of caspase 1 is the main source of IL-1β production and secretion although caspase 1 independent proteolysis of pro- IL-1β has been reported (10). Upon activation, NLRP3 is phosphorylated by the licensing NIMA-related kinase 7 (NEK7) and undergoes drastic conformational changes from a closed inactive state to an open, oligomeric, and active conformation (11–13). In the latter, the central N-terminal pyrin domains bind and oligomerize the downstream adapter ASC (14, 15). In turn, ASC recruits caspase 1 into the complex via CARD-CARD interactions (16). Subsequently, caspase 1 undergoes activation by autocleavage which allows for proteolytic processing of pro- IL-1β to biologically active IL-1β. IL-1β is released from the cell by exocytosis of secretor lysosomes (17, 18) or in the context of proinflammatory cell death termed pyroptosis (19).

We have recently shown that a short accessory peptide (PB1-F2) encoded by segment 2 of IAV (H5N1, H7N9, and H3N2) could act as an inhibitor of NLRP3 activation, pro-IL-1β cleavage, and pyroptotic cell death of infected macrophages (20). Mechanistically, PB1-F2 prevents the interaction of NEK7 with the LRR domain of NLRP3 maintaining NLRP3 in an inactive confirmation. Importantly, not all IAV strains express a full-length PB1-F2 and some of those which do, do not antagonize NLRP3 activation.

Here, we took advantage of two IAV strains with differential PB1-F2-NLRP3 interaction phenotypes. A/Puerto Rico/8/1934 (PR/8, H1N1) PB1-F2 binds poorly to the LRR of human NLRP3, while A/Viet Nam/1203/2004 (VN/1203, H5N1) PB1-F2 shows robust binding and inhibition of NLRP3 signaling. With a combination of sequence comparison and Alphafold2- guided structure prediction, we identified a sequence motif within the C-terminal half of PB1-F2, which is necessary and sufficient for NLRP3 LRR interaction and required for subsequent proinflammatory responses.

RESULTS

We had previously shown that full-length PB1-F2 of contemporary H3N2 [A/Wyoming/03/2003 (Wy/03)], H5N1 [A/Viet Nam/1203/2004 (VN/1203)], and H7N9 [A/Shanghai/1/2013 (SH/1)] viruses coprecipitate human NLRP3(20). Mostly, this interaction relies on the C-terminal 50aa of PB1-F2. Both the pyrin domain (PYD) and the LRR domain (LRR) serve as anchor point for the interaction with PB1-F2 (20). In consequence, PB1-F2-deficient mutants of VN/1203 and Wy/03 induced higher levels of IL-1β in infected human macrophages. In contrast, PB1-F2 of A/Puerto Rico/8/1934 (PR/8) only poorly interacted with human NLRP3 (20). We decided to take advantage of this differential binding to human NLRP3 to identify the NLRP3-binding motif of PB1-F2.

A multiple sequence alignment of the amino acid sequence of PB1-F2 of PR/8, Wy/03, VN/1203, and SH/1 revealed three regions with distinct sequences, differentiating NLRP3 binding (Wy/03, VN/1203, and SH/1) from the non-binding PB1-F2 (PR/8). We labeled them from N-terminus to C-terminus as motif I, II, and III (Fig. S1A). We next used Alphafold2 (21, 22) to predict the structure of a VN/1203 wt PB1-F2–NLRP3 complex. To increase the predictive power, we removed the flexible N-terminus of PB1-F2 and modeled it to a recently published NLRP3 structure with a short N-terminal truncation (13). The best model predicted interaction of VN/1203 PB1-F2 C-terminal peptide (aa40-90) with the concave surface of the NLRP3 LRR, overlapping with the already published NEK7 interface (13) (Fig. S1B). When analyzing predicted hydrogen bonds between PB1-F2 C-terminal peptide and NLRP3 LRR, we found two in motif II and one from motif III (Fig. S1A).

To test these findings biochemically, we decided to swap all three motifs between VN/1203 PB1-F2 C-terminal peptide (VN Cterm) and PR/8 PB1-F2 C-terminal peptide (PR8 Cterm) and perform co-immunoprecipitation experiments with the PYD and the LRR of NLRP3. V5-tagged NLRP3 PYD or LRR were co-expressed with the different permutations of the PB1-F2 C-terminal peptide (aa40-90) fused to ZsGreen (Fig. 1C; Fig. S1C). This N-terminal tag is required to stabilize the short PB1-F2 peptide. To study the contribution of the central motif I, we constructed additionally an N-terminal and a C-terminal fragment of VN/1203 PB1-F2 with or without the permutation to the corresponding PR/8 sequence (Fig. 1C). We previously showed that the C-terminal peptide of VN/1203 PB1-F2 more efficiently pulls down full-length human NLRP3 as compared to the N-terminal peptide of PB1-F2(20). Here, we show that the same holds true for the individual domains of human NLRP3. Only the C-terminal constructs interacted robustly with the PYD and the LRR domain. Substitution of the motif I of VN/1203 with the sequence of PR/8 did not alter the pulldown efficacy for either domain of human NLRP3 (Fig. 1A and B). We next focused on the C-terminal region of PB1-F2. Deletion of the three C-terminal amino acids of VN PB1-F2 (WIN, motif III) did not affect the interaction of the VN/1203 PB1-F2 C-terminal portion with the LRR and potentially impacts PYD binding although not to a statistically significant level ($P = 0.107$). Importantly, a permutation of the TQGS motif (II) into ILVF reduced interaction with the PYD and the LRR of NLRP3 to background levels (Fig. 2A and B). To show the specificity of this improved interaction, we also performed the inverse pulldown experiment using V5-tagged PYD and V5-tagged LRR (Fig. 1C; Fig. S2A and B).

We would like to point out that permutations of PB1-F2 Cterm motifs affected the total protein levels of co-expressed LRR, as shown in the whole-cell lysates (WCL in Fig. 2A and B). In the western blot quantification, we adjusted for these differences by normalizing the signal in the IP to the signal of the WCL. Our results suggested that the TQGS motif (aa68-71) is required for efficient binding of PB1-F2 to the LRR domain of NLRP3. We next asked if the presence of this motif would be sufficient for the interaction. We permutated the ILVF motif in PR/8 PB1-F2 (Cterm peptide) to TQGS and repeated the co-immunoprecipitation experiments. The WT construct of PR/8 did not coprecipitate with the PYD and only poorly with the LRR domain. Importantly, introduction of the TQGS motif of VN/1203 PB1-F2 was sufficient to permit co-precipitation of the PYD and significantly improved interaction with the LRR (Fig. 2C and D). The TQGS motif (motif II) is also important in the context of full-length PB1-F2 interacting with full-length human NLRP3 (Fig. 3A and B). As for the shorter constructs of PB1-F2, we observed a clear reduction in the amounts of PB1-F2 full length when a TQGS motif was present (see whole-cell lysates) (Fig. 3A). Importantly, these peptides still pulldown full-length NLRP3 more efficiently than their ILVF carrying counterparts (Fig. 3B).

To support the relevance of our findings, we addressed how prevalent the ILVF and the TQGS motifs are in different influenza A virus-host species. We limited our analysis to those isolates encoding a full-length (87–90 amino acid) PB1-F2. A comparison of more than 35,000 non-redundant sequences from the NCBI Influenza Research database showed a high prevalence of the TQGS motif in humans, especially between 1968 and 2003 (Fig. S3A). In recent years, a TQVS motif as found in Wy/03 PB1-F2 was dominant, which also antagonizes human NLRP3(20). The ILVF motif was found in isolates from 1933 to 1957. In swine isolates, TQGY was the most prevalent sequence variation found in recent isolates (Fig. S3B). In avian isolates, TQES was mostly reported in the last 30 years, followed by TQGS (Fig. S3C). Interestingly, the first two amino acids (TQ), which form additional H-bonds in the alphafold 2 prediction of the NLRP3-PB1-F2 complex (Fig. S1B), show the highest conservation across host species. Of note, Fig. S2 shows relative numbers and very few isolates are reported from the early 20th century, some of which with a long history of laboratory passages.

We next tested if exchange of the terminal tryptophan residue of NLRP3 for alanine would affect PB1-F2 interaction. This single amino acid swap did not affect interaction with PB1-F2 suggesting that the interface on the NLRP3 side is more complex (Fig. S4).

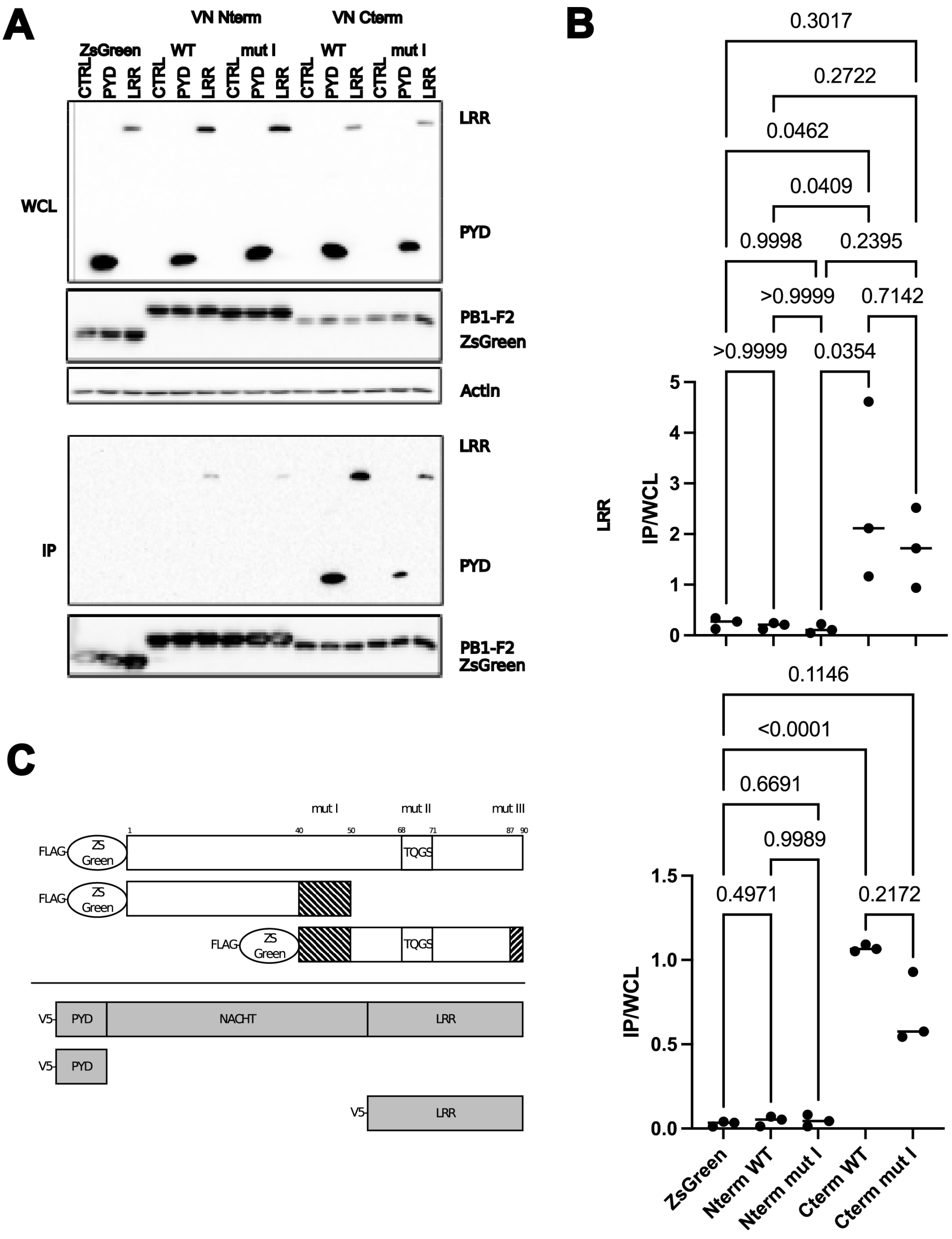

FIG 1 (A) Coimmunoprecipitation of human NLRP3 LRR or PYD (V5 tagged) with different VN/1203 PB1-F2 N and C-terminal peptides containing permutations in motif I. Representative blots are shown. (B) Quantification of band intensity in three independent experiments. Band intensity of IP samples over WCL samples was calculated. Statistical significance was determined by one-way ANOVA, and *P*-values are indicated. (C) Schematic representation of PB1-F2 and NLRP3 constructs with the positions of mutations indicated (from top to bottom): full-length PB1-F2 (FL), N terminus PB1-F2 (aa 1–50), C terminus of PB1-F2 (aa 40–90), human NLRP3 (NLRP3 WT or W1034A), NLRP3 pyrin domain (PYD), and NLRP3 LRR domain (LRR). Of note the matching WT constructs are not depiced. All PB1-F2 constructs are fused to ZsGreen at the N-terminus and carry an N-terminal FLAG tag. All NLRP3 constructs are fused to V5 tag at the N-terminus [ref].

Early work on PR/8 PB1-F2 suggested that the ILVF motif overlaps with the mitochondrial targeting sequence (MTS), which spans from aa69-82 (23). To address, if a swap of the TQGS motif would affect subcellular localization and/or colocalization with NLRP3 we performed co-expression experiments of ZsGreen-tagged C-terminal peptides of PB1-F2

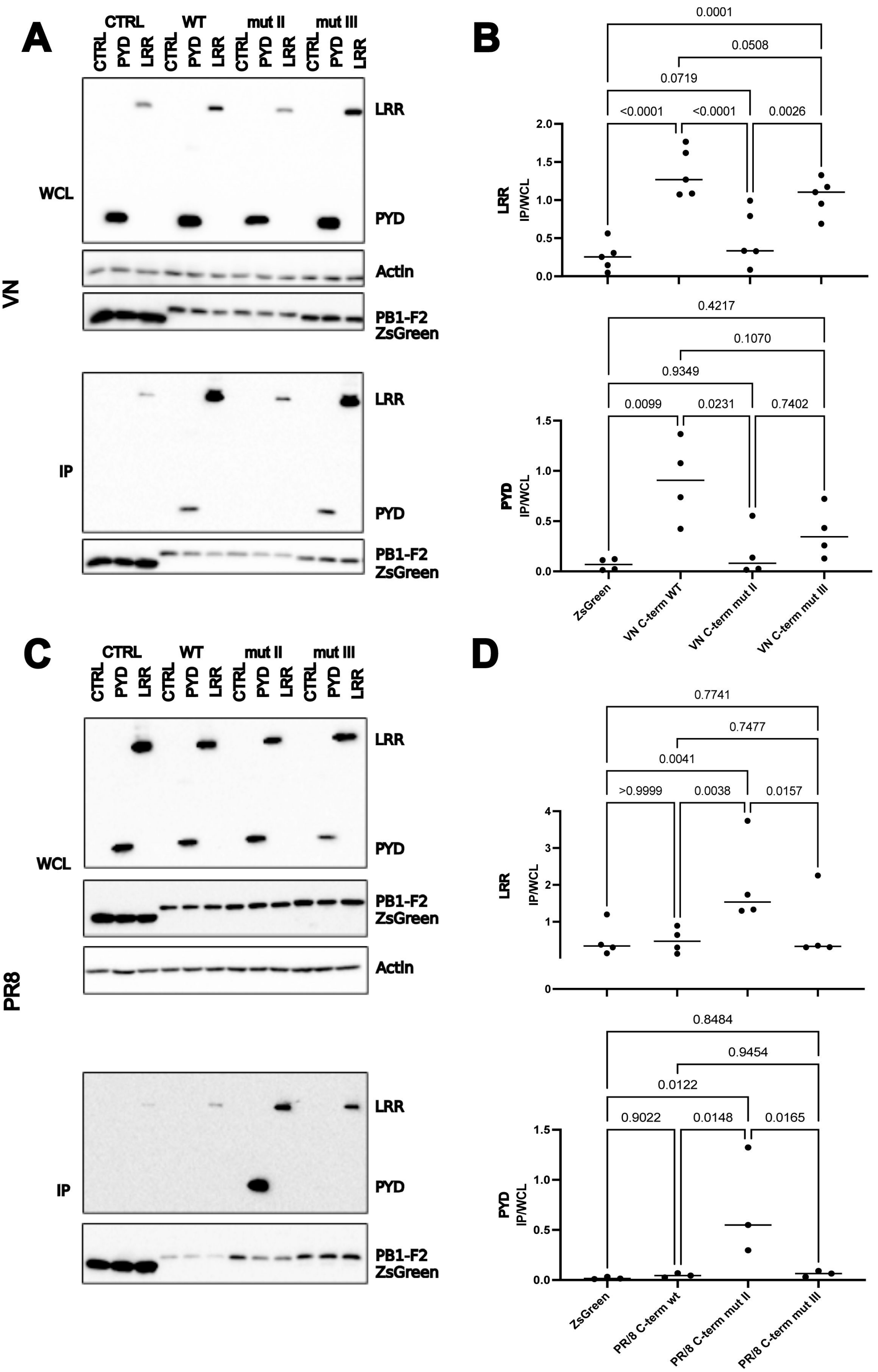

FIG 2 (A) Coimmunoprecipitation of human NLRP3 LRR or PYD (V5 tagged) with different VN/1203 PB1-F2 C-terminal peptides containing permutations in motif II and III. Representative blots are shown. (B) Quantification of band intensity in five independent experiments. Band intensity of IP samples over WCL samples was calculated. Statistical significance was

(Continued on next page)

FIG 2 (Continued)

determined by one-way ANOVA, and *P*-values are indicated. (C) Coimmunoprecipitation of human NLRP3 LRR or PYD (V5 tagged) with different PR/8 PB1-F2 C-terminal peptides containing permutations in motif II and motif III. Representative western blots are shown. (D) Quantification of band intensity in four independent experiments. Band intensity of IP samples over WCL samples was calculated. (C) Quantification of band intensity in three independent experiments. Band intensity of IP samples over WCL samples was calculated. Statistical significance was determined by one-way ANOVA, and *P*-values are indicated.

with a V5-tagged PYD or LRR of human NLRP3. The localization of NLRP3 (red signal) was identical, independent of the PB1-F2 variant that was co-expressed. The VN1203 PB1-F2 WT C-terminal peptide colocalized in distinct puncta with the NLRP3 LRR throughout the cell body (Fig. S5A, upper four pictures). Permutation of the TQGS motif to ILVF resulted in a focusing of the ZsGreen signal in the perinuclear region, mostly in larger patches, which did not colocalize systematically with the LRR signal. In contrast, the localization of PR/8 PB1-F2 WT peptide resembled that of the mutant VN/1203 (larger patches in the perinuclear region) without colocalization with the LRR. However, it is noteworthy

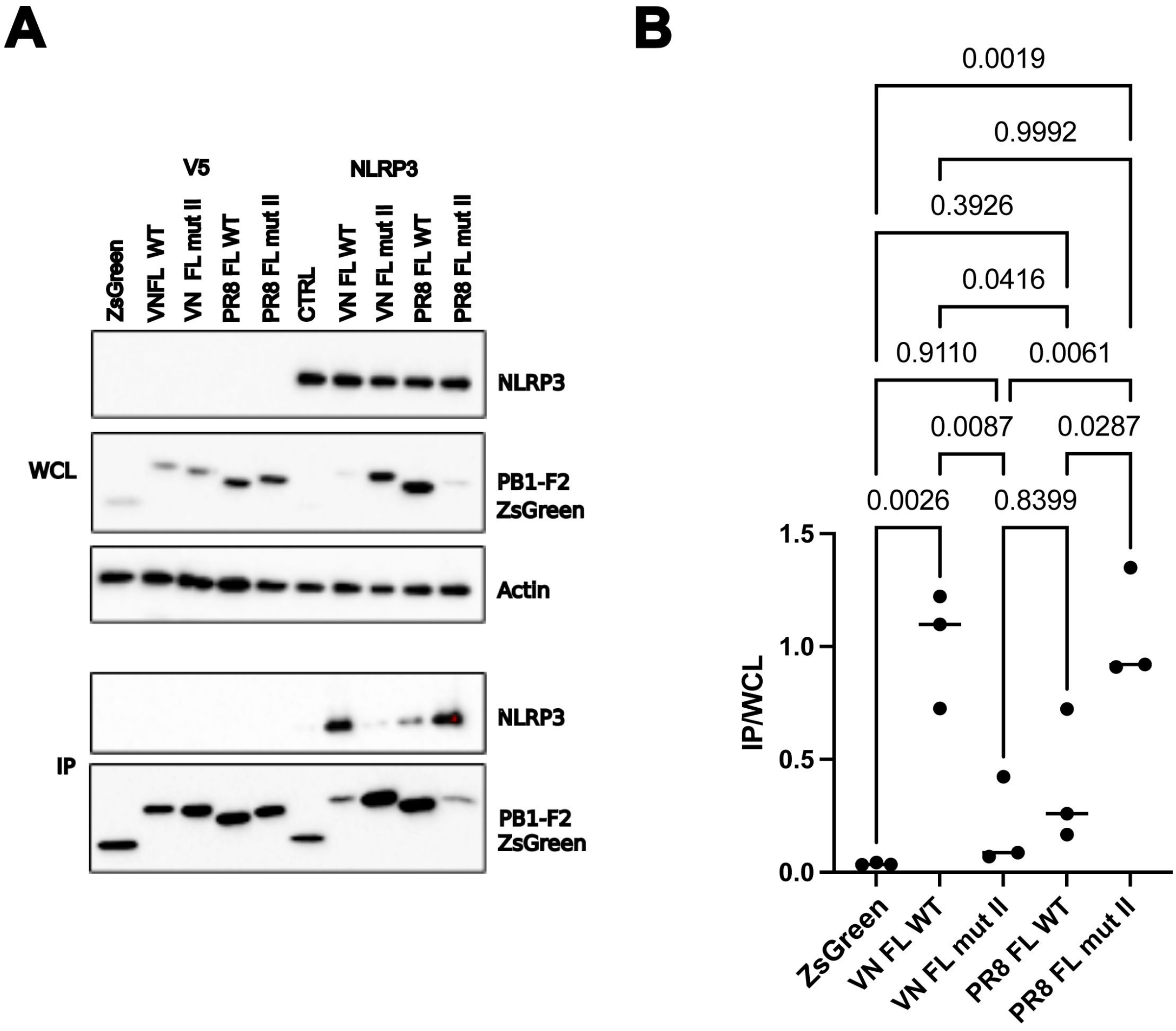

FIG 3 (A) Coimmunoprecipitation of full-length human NLRP3 (V5 tagged) with different full-length PB1-F2 (from PR/8 or VN/1203) containing permutations in motif II. Representative blots from five independent transfection/pulldown experiments are shown. (B) Quantification of band intensity in five independent experiments. Band intensity of IP samples over WCL samples was calculated. Statistical significance was determined by one-way ANOVA, and *P*-values are indicated.

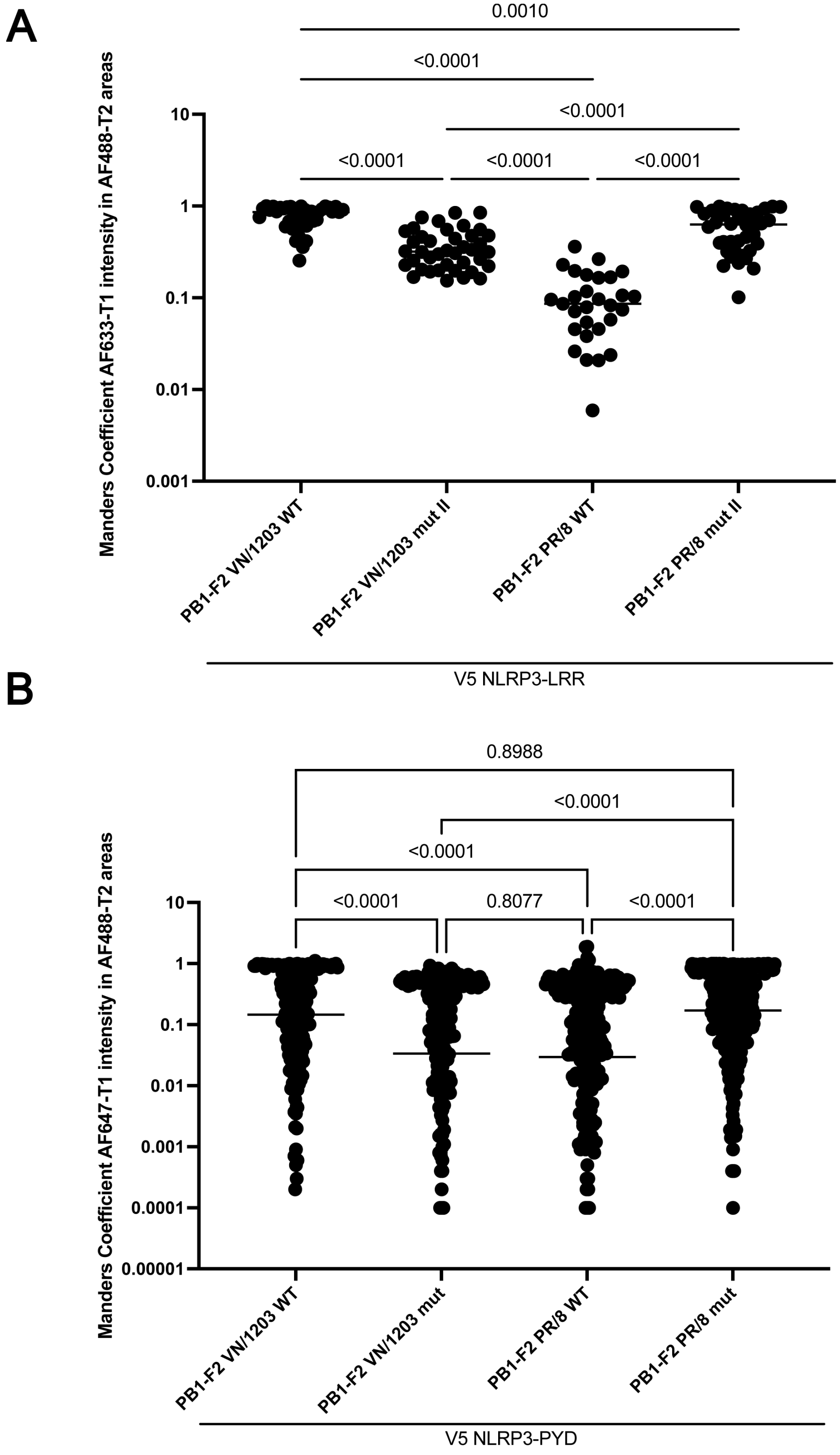

FIG 4 C-terminal peptides of PB1-F2 of VN/1203 or PR/8 with or w/o permutation of motif II were co-expressed with the LRR domain (A) or the PYD (B) of human NLRP3 in HeLa cells. Cells were imaged by confocal laser scanning microscopy. Representative pictures are shown in Fig. S5. Quantification of PYD or LRR-PB1-F2 colocalization in 24 randomly chosen frames (Continued on next page)

FIG 4 (Continued)

from three independent experiments. Each dot represents the calculated overlap of NLRP3 domain signal with that of the PB1-F2 signal in the cytoplasm of a double-transfected cell. Statistical significance was determined by one-way ANOVA, and *P*-values are indicated.

that most cells expressed very small amounts of PR/8 PB1-F2 WT. Introduction of the TQGS motif resulted in broader distribution of the PB1-F2 signal in smaller puncta and colocalization with the LRR signal. An unbiased analysis of colocalization of PB1-F2 signal with that of the NLRP3 LRR in randomly chosen frames confirmed these observations (Fig. 4A). Notably, PR/8 PB1-F2 Cterm WT colocalized still less with the NLRP3 LRR than VN/1203 PB1-F2 C-term ILVF mutant, suggesting that the colocalization is, in part, driven by additional sequences in VN/1203 PB1-F2 Cterm. We performed the same colocalization experiments with the PYD of human NLRP3 and found that generally the PYD colocalized substantially less with the respective PB1-F2 constructs (Fig. S5B; Fig. 4B). Nevertheless, the colocalization followed generally the same pattern as observed for the colocalization of PB1-F2 Cterm and LRR (more colocalization if a TQGS motif was present than if an ILVF motif was present).

Next, we asked, if the exchange of the TQGS for a ILVF motif would affect the replication capacity of VN/1203 influenza A virus. To test this hypothesis, we performed a multicycle growth curve in a relevant tissue model; human precision cut lung slices (PCLS). These volume-defined tissue discs cut from healthy tumor bystander tissue of fresh lung resections, preserve the natural cell composition and 3D-architecture of lung tissue, and constitute, thus, a highly relevant preclinical model (24). PCLS from tissue of three human patients (Table S1) were infected with VN/1203 WT virus or the VN/1203 PB1-F2-ILVF. The two viruses replicated identically in a multicycle growth curve in these tissues, suggesting no inherent replication defect even in the absence of NLRP3 antagonism (Fig. 5A). This is supported by the protein levels of viral proteins found in infected THP-1-derived macrophages. As for the recombinant PB1-F2 constructs, the TQGS carrying PB1-F2 was present in lower levels as the ILVF variant (Fig. 5B).

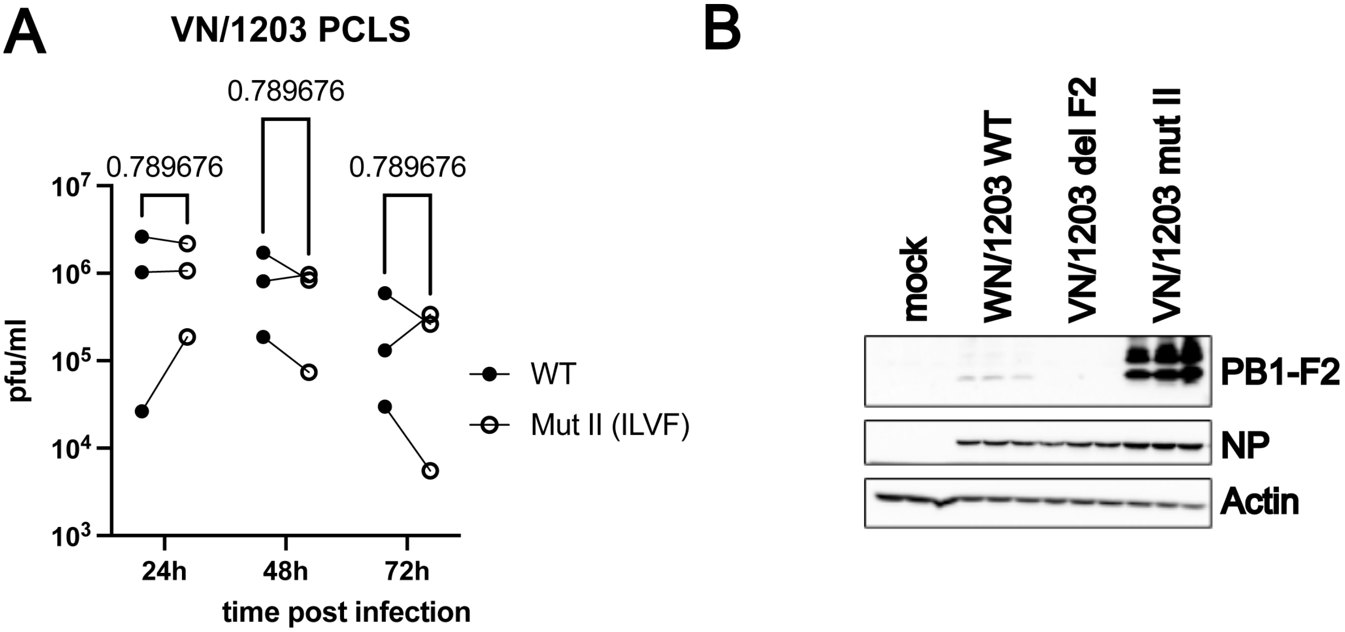

FIG 5 (A) Precision cut lung slices from three human patients were infected with 10^5 pfu of VN/1203 WT or VN/1203 mut II (ILVF) virus. Virus titers were determined by standard plaque assay after 8, 24, 48, and 72 h from the supernatants. Statistical significance was determined by one-way ANOVA, and *P*-values are indicated. (B) THP1-derived macrophages were infected with the indicated viruses and indicated viral proteins were detected after 24 h of infection. Samples from three independent experiments are shown side by side.

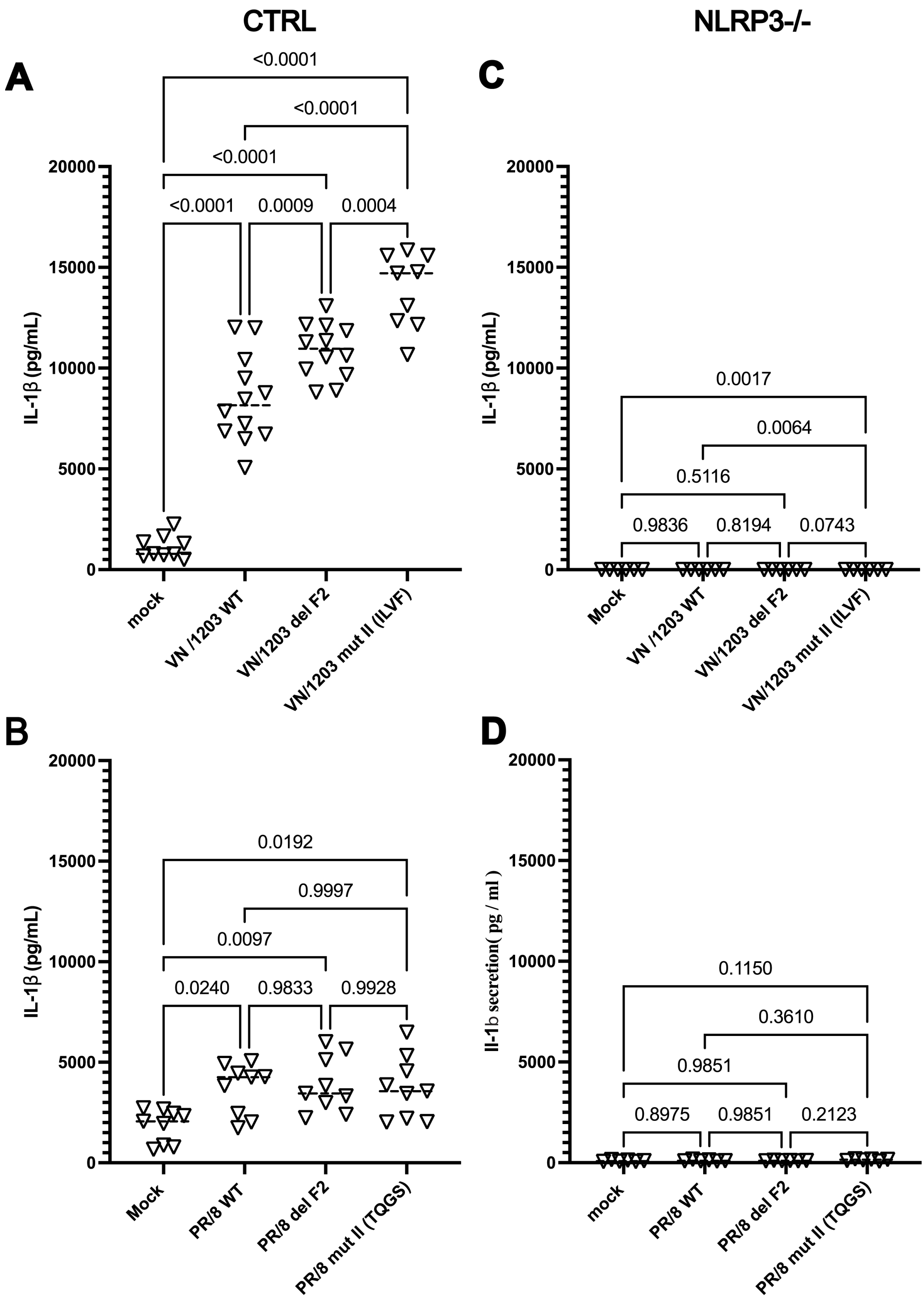

FIG 6 (A and B) THP-1-derived macrophages were infected for 18 h with 10 MOI of VN/1203 (A) or 50MOI of PR/8 viruses (B). IL-1β from three or four independent experiments (with two biological repeats each) was quantified by specific ELISA against a predefined standard curve. (C and D) THP-1 NLRP3–/–derived macrophages were infected for 18 h with 10 MOI of VN/1203 (C) or 50MOI of PR/8 viruses (D). IL-1β from two independent experiments was quantified by specific ELISA against a predefined standard curve. Statistical significance was determined by one-way ANOVA, and *P*-values are indicated.

Importantly, THP-1-derived macrophages produced significantly more IL-1β when infected with VN/1203-PB1-F2-ILVF mutant virus than with the isogenic WT strain. Induction levels were comparable to those of VN/1203 PB1-F2-deficient strain (Fig. 6A). The IL-1β secretion after VN/1203 infection was fully dependent on NLRP3 since NLRP3-deficient THP-1-derived macrophages released no detectable IL-1β (Fig. 6B). Infected PCLS did not secrete measurable amounts of IL-1β (data not shown). Since these tissues are disconnected from a functional circulation, proinflammatory monocytes cannot be recruited, which are the main source of IL-1β. Surprisingly, the introduction of a TQGS motif into PR/8 PB1-F2 did not suppress IL-1β secretion from infected macrophages, as one could have assumed. We would like to stress that PR/8 is a quite poor inducer (or very good controller) of IL-1β release from human macrophages as compared to VN/1203, which might make it more difficult to show a reduction of IL-1β production by PB1-F2 mutation (Fig. 6C). To reach comparable induction of IL-1β, it requires a fivefold higher infectious dose (50 MOI) as with VN/1203. As for VN/1203, PR/8 induced IL-1β in an NLRP3-dependent fashion (Fig. 6D). When testing for induction of IP10, ISG15, MX1, or CCL5, we did not see enhanced expression related to the here described PB1-F2 mutant. Rather VN/1203 mutII (ILVF) virus appears to induce less antiviral responses than the matching WT strain (Fig. S6).

DISCUSSION

PB1-F2 function is highly strain and cellular context dependent [reviewed in reference (25)]. Early findings described it as a proapoptotic and proinflammatory accessory protein of influenza A virus (26, 27). In part, this observation relies on the presence of a mitochondrial targeting signal (MTS) in the C-terminus of PB1-F2, as for example found in PR/8 PB1-F2. Leucine residues within the C-terminal region of PB1-F2 are essential for the mitochondrial localization (23). These peptides penetrate the inner mitochondrial membrane and perturb the mitochondrial membrane potential, ultimately resulting in apoptosis (23, 26). CD spectroscopy of PB1-F2-derived peptides and NMR data suggest that the C-terminal region of PR/8 PB1-F2 forms an continuous alpha-helix (28). Importantly for H5N1 PB1-F2s, this MTS is disrupted leading to a rather cytoplasmic distribution (27). Comparison to the PB1-F2 of a H5N1 from 2000 revealed a loop region from aa66-71, disrupting the alpha-helix (28). This was proposed to rely on the helix-breaking features of T, G, and S as compared to the helix-forming residues L and F (28). The TQGS motif identified here is overlapping with this MTS. Accordingly, we found here a distinct subcellular distribution of VN WT and ILVF mutant PB1-F2. It is currently unclear if the leucin residue of the ILFV motif of PR/8 PB1-F2 contributes to subcellular localization. In line with our results, recent work demonstrated that PR/8 PB1-F2 changes subcellular localization upon exchange of the ILVF motif to a TQDS motif (29), although in this study PR/8 PB1-F2 coupled to EGFP moved from the mitochondria to the nucleus, when containing the TQDS motif. Amino acids 68–70 of PR/8 PB1-F2 were also assigned to the cytotoxic effects of PB1-F2-derived peptides (30). In line with this, the ILV motif of PR/8 was shown to contribute to its proapoptotic function in context of infection, which was not found for the ancestral 1918 H1N1 strain (27). The sequence composition of motif II might hence define if PB1-F2 acts as antagonist of the interferon response/cytotoxic peptide (ILVF) or as inhibitor of the proinflammatory host response (TQGS). This would, in part, resolve contradictory findings on the role of PB1-F2 on regulating host responses. However, sequences outside of motif II clearly also contribute to the immune modulatory function of PB1-F2. Notably, PB1-F2 of H7N9 was shown to prevent NLRP3-MAVS-interaction, eventually leading to reduced IFNβ production (31). Suppression of MAVS signaling could depend on an LIR motif (W/Y ×× I/L, aa61-64) in the C-terminus of PB1-F2, required for induction of mitophagy (32). A comparative study found that an H3N2 viruses with a truncated 11aa PB1-F2 induces lower levels of ISGs and proinflammatory cytokines in human lung epithelial cells, while a H7N1 virus with the same PB1-F2 truncation induced a comparable antiviral response as the isogenic WT strain (33). Work on H3N2-expressed PB1-F2 identified proinflammatory markers (residues 62, 75, 79, and 82), which do not overlap with the TQGS motif (34). Sequences outside of motif II might hence explain why the ILVF-TQGS substitution in PR/8 did not result in an enhanced IL-1β production. We further cannot rule out that PR/8 has alternative means to limit inflammasome activation. For a closely related virus (A/WSN/1933), the non-structural protein 1 was shown to inhibit NLRP3 activation (35). The addition of the TQGS motif in PB1-F2 might in consequence just provide a redundant NLRP3 antagonism.

Interestingly, recent studies suggest that PB1-F2 requires to form macromolecular aggregates to exert defined biological functions (36). Importantly, phagocytosed extracellular PB1-F2 macromolecules activate NLRP3, while intracellular PB1-F2, e.g., in virus-infected macrophages, could block NLRP3 activation, albeit the mechanism is still under debate (37). This might explain why cell culture models using PB1-F2 C-terminus-derived peptides often generate proinflammatory outcomes (27, 36, 38, 39).

Our work adds an additional piece to the puzzle of PB1-F2 functions, by defining a molecular interface required for the inhibition of human NLRP3 action. Our phylogenetic analysis does, however, suggest that not all PB1-F2s harbor this feature. More importantly, it is well described that human H1N1 viruses descending from the 1918 lineage lost their PB1-F2 ORF due to introduction of a premature Stop codon (40). Similarly, the 2009 pandemic H1N1 strains only expressed a highly truncated 11aa PB1-F2 and reinstallation of the PB1-F2 has only minimal effect of viral pathogenicity (41). It is currently unclear, why certain IAV strains thrived successfully in the human population without expressing a full length PB1-F2 ORF. A functional redundancy with other accessory proteins (e.g., NS1), might explain this development.

The understanding of NLRP3 inflammasome assembly was boosted by a series of recent landmark cryo-EM work (13, 42–45). It was proposed that NLRP3 transits from a monomeric inactive state via an oligomeric cage-intermediate to a NEK7 bound, flower-shaped oligomer in which the LRRs with bound NEK7 form the petals and the PYD the beginning of the stem, where ASC will oligomerize (42). In this model, NEK7 binding to LRR opens the oligomeric cage at the microtubule organization center (MTOC). Our data open two mutually possible mechanisms of action for PB1-F2-dependent inhibition of NLRP3 inflammasome activation: (i) via repression of LRR-LRR interaction and cage formation at the *trans* Golgi network and/or (ii) via suppression of LRR NEK7 interaction at the MTOC.

In summary, we identified here by rational mutagenesis a binding patch of four amino acids in the C-terminus of contemporary IAV PB1-F2, that is necessary and sufficient for the binding and inhibition of human NLRP3 function.

Limitations of this study

We do not provide co-immunoprecipitation or colocalization experiments for PB1-F2 (WT or mut) with endogenous NLRP3 from IAV-infected macrophages to show interaction in context of a relevant model. The specificity of PB1-F2 antibodies does not allow this type of experiments. However, since we find a functional phenotype in infected macrophages (IL1-beta secretion changes) and see a similar effect of our motif II mutations on PB1-F2 stability, we believe that our pulldown experiments in HEK293T cells are relevant and meaningful.

MATERIALS AND METHODS

Plasmids

Expression plasmids for Flag-ZsGreen-PB1-F2 constructs (Nterm, Cterm, or full length) for VN/1203 and PR/8 were generated by cloning the coding region for the C-terminal 50aa of VN/1203 PB1-F2 (or 47 for PR/8), via NheI and XhoI into pCAGGS-Flag-ZsGreen (46). Overlapping oligonucleotides containing the permutations for motif I-III were used to generate the ZsGreen-PB1-F2-C-term mutant constructs for VN/1203 and PR/8 in pCAGGS-Flag-ZsGreen (46) or in pDZ for generation of replicating recombinant IAV. Oligonucleotides are listed in Table S2. Expression plasmids for V5-tagged domains of human NLRP3 were published earlier [ref]. The W1034A substitution was verified by Sanger sequencing (Microsynth). None of the changes introduced in PB1-F2 affected the PB1 ORF (for recombinant viruses).

Oligonucleotides

Oligonucleotides were custom synthesized by Microsynth. Sequences are listed in Table S2.

Antibodies

An anti-VN/1203 PB1-F2 antiserum was generated by challenging rabbits with the N-terminal 30aa of PB1-F2 VN/1203 coupled to KLH (47). The following commercial antibodies and antisera were used: rabbit polyclonal anti-influenza virus NP (Invitrogen, Cat#PA5-32242), anti-actin-HRP (Abcam, Cat# ab49900), mouse anti-Flag-HRP (Sigma; Cat# A8592), mouse anti-V5-HRP (Invitrogen #46-0708), goat polyclonal anti-rabbit-HRP (Sigma-Aldrich, Cat#A8275).

Cells

HEK 293T cells (Human embryonic kidney) were obtained from ATCC. MDCK II cells were a kind gift from Dr. Silke Stertz, University of Zurich. Both were cultured in DMEM (Dulbecco's modified Eagle medium, Gibco) supplemented with 10% heat-inactivated fetal bovine serum (FBS) (Gibco) and 1% penicillin–streptomycin (Pen-Strep) (Sigma-Aldrich). THP-1 CTL or NLRP3−/− cells were kindly provided by Dr. Veit Hornung LMU, Munich, Germany (11) and were cultured in RPMI 1640 media complemented with 10% FBS, 1% Pen-Strep, and 1% sodium pyruvate (Gibco). All cells were incubated at 37°C with 5%CO_2 and 90% humidity.

Precision cut lung slices

PCLS were generated in line with published protocols (1, 2). Briefly, healthy human lung tissue was obtained from bystander material of tumor resections of three patients. The airways were perfused with 2% low melting agarose and tissues were rested for 30 min at 4°C. 8 mm ∅ tissue cores were generated with an electric coring press and transversely cut into 250 µm thick PCLS with a MD6000 Krumdieck tissue slicer in cold PBS (both instruments Alabama Research and Development). PCLS were cultured in 24-well plates with DMEM F-12 supplemented with antibiotics (100 U/mL penicillin and 100 µg/mL streptomycin, w/o fetal bovine serum) at 37°C, 5% CO_2, and 95% humidity for 24 h before the experiment. For PCLS from each patient, two independent sets of infections were performed in biological triplicates. Supernatants of PCLS were collected at indicated time points, and viral titers were determined by standard plaque assay on MDCK cells.

Cell differentiation and stimulation

THP-1 human monocytes were differentiated into adherent macrophage-like cells by treatment with 0.5 µM of PMA (Phorbol 12-myristate 13-acetate) (Sigma-Aldrich) for 3 h at 37°C, washed once in PBS (Gibco), and seeded at 1×10^6 cells/mL (12 well plate) in complete media overnight. As a positive control for inflammasome activation, differentiated THP-1 cells were treated with 6.7 µM of nigericin.

Transfection

Sub-confluent HeLa cells or HEK293T cells were transfected with LT-1 (Mirrus) transfection reagent according to the manufacturers protocol using a 2:1 ratio of LT-1 : DNA. For Co-immunoprecipitation of PB1-F2 with NLRP3 cells were cultured in the presence of MG132 (10 µM for 5 h) to limit proteasomal degradation of PB1-F2.

Western Blot and co-immunoprecipitation

Cells were lysed with RIPA buffer (50 mM Tris-HCl pH7.5, 150 mM NaCl, 0.5 mM EDTA, 0.5% NP-40 containing a protease inhibitor cocktail (Thermo Scientific #A32965) and mechanically disrupted by ultrasonication (Diagenode Bioruptor) adjusted to 10× cycles of 30 s. Cell debris was pelleted by centrifugation at 10,000 × *g* for 15 min at 4°C. Flag or V5-tagged proteins were precipitated with anti-flag or anti V5 agarose beads (Merck). Cell lysates or eluted proteins from co-immunoprecipitations were mixed with urea sample buffer (6 M urea, 2 M β-mercaptoethanol, and 4% SDS) and separated electrophoretically on 7.5%, 10%, or 15% SDS-polyacrylamide gels. Proteins were transferred to nitrocellulose membranes (0.45 µm), and proteins were detected with specific antibodies. Secondary HRP-coupled antibodies were used to visualize protein bands with ECL substrate. Band intensity was quantified using ImageJ and the signal obtained from IP samples was normalized over the corresponding input control.

Confocal fluorescence microscopy

HeLa cells were seeded on sterile glass cover slips. Sub-confluent HeLa cells were transfected with ZsGreen-PB1-F2 C-term (250 ng for VN C-term WT, VN C-term ILVF, and PR8 C-term TQGS; 1,000 ng for PR8 C-term WT) and V5-NLRP3 LRR expressing or V5-NLRP3 PYD plasmids (500 ng). Twenty-four hour post transfection cells were stained fixed (for 120 min) with 4% formaldehyde and permeabilized with 0.1% Triton-X100 in PBS (for 15 min). Cells were blocked with PBS with 1% BSA for 1h340 at RT and stained with anti-V5 antibody (EV/V4RR, Invitrogen) (10 µg/mL in blocking solution) for 1 h. Cells were washed three times with PBS with 1% BSA (within 35 min, for 5 min per wash) and stained with a goat anti-mouse AF 647 (Invitrogen) (5 µg/mL) for 1 h. Cells were washed three times with PBS with 1% BSA (within for 5 min per wash), followed by two washes with PBS. Cover slips were mounted with ProLong mounting medium with DAPI (Invitrogen) and sealed with nail polish.

Confocal images were acquired using a Zeiss Axio Imager.Z2 Basis LSM 800 microscope, with objective Plan-Apochromat 63×/1.40 Oil DIC M27 and software ZEN2.3. Wavelengths of excitation and emission were 631/647, 493/517, and 353/465. Eight fields in which positive cells for transfection with both plasmids were imaged per experiment ($n = 3$).

Image analysis was performed with QuPath (48) 0.4.2 and 0.3.2 and Cellpose (49) algorithm to detect cells and nuclei under the supervision of the user. The percentage of ZsGreen-PB1-F2 C-term that colocalized with V5 NLRP3-LRR in the cytoplasmic area was determined using Manders' coefficient (50) with the same user-defined thresholds per channel, across all experimental conditions. Scripts for analysis of confocal images can be found in the supplementary material and methods section (Script 1 and 2).

ELISA

Human IL-1β was quantified from cell culture supernatants using a BD OptEIA Human IL-1β Elisa Set II #557953. Assays were performed on Nunc - Immuno plates (Thermo scientific) according to the manufacturer's instructions (BD Biosciences). Captured cytokines were quantified against a serially diluted standard by reading absorbance (*A* 450 nm) values in a Thermo Scientific Multiskan GO. Analysis was done using the four - parameter logistic ELISA curve.

Plaque assay

Infectious viral titers were determined by standard plaque assay (51). Briefly, virus-containing tissue culture supernatant was precleared from cellular debris for 2 min at 2,000 × *g*. Supernatants were stored at −70°C until analyzed. Samples were thawed on ice and diluted in 10-fold steps in PBS containing 0.2% BSA and pencillin/streptomycin. Confluent MDCK II cells were infected with 200 µL of virus dilution in a 6-well for 45 min while rocking the plates every 10 min. Residual supernatant was aspirated, and cells were washed once with PBS and overlayed with 2% low melting agar in infection medium. MDCK II cells were fixed with 4% formaldehyde solution and stained with crystal violet. Infectious titers were calculated as pfu/mL by multiplication of plaque counts with dilution factor and volume.

PB1-F2 sequence analysis

87–90 aa non-redundant PB1-F2 sequences from human, swine, and avian hosts were extracted in March 2023 from the NCBI Influenza Virus Resource Database (https://www.ncbi.nlm.nih.gov/genomes/FLU/Database/nph-select.cgi?go=database). Motif II sequence composition was plotted against the isolation year as relative sequence abundance.

Multiple sequence alignment

PB1-F2 peptide sequences of PR/8 (YP_418248.1), Wy/03 (ACF54574.1), VN/1203 (ADD97093.1), and SH/1 (EPI439489) were retrieved from NCBI or GISAID and aligned with Clustal Omega (version 1.2.4) (https://www.ebi.ac.uk/Tools/msa/clustalo/) (52, 53).

Motif extraction

We downloaded 30,000 + full length (87–90aa) PB1-F2 sequences from NCBI Influenza virus resource and wrote Python scripts to extract non-redundant sequences. The first script (Script 3) “unique_seqs.py” used fasta files downloaded from the NCBI Influenza Virus Resource Database (full length only) for each host and created two files; a first .fasta file (1) containing all unique sequences and a second tabulated file (2) showing the identifiers for each individual sequence. The fasta file (1) containing unique sequences served as input to “Clustal Omega” (version 1.2.4) with default parameters yielding multiple alignment file (3). The second script “motif_extract.py” (Script 4) used as input alignment file (3) and tabulated file (2) to generate a new fasta file containing all individual motives and a tabulated file recapitulating the motives. The counts for each motif permutation were then plotted against the isolation year as relative percentage.

Structure prediction

The models of the protein-protein interactions between NRLP3 (amino acid 61–1036 of NP_004886) and PB1-F2 (amino acid 40–90 of ADD97093.1) were generated using ColabFold v1.5.2 notebook (54) using the default settings with Amber relaxing (msa_method = mmseqs2_uniref_env ; pair_mode = unpaired_paired ; max_msa = 512:1024 ; subsample_msa = True ; num_relax = 1 ; max_recycles = 24 ; tol = 0.5 ; template_mode = pdb70 ; use_amount = num_relax > 0). All models with an overall pLDDT (predicted local distance difference test) value less than 70 were ignored. Analyzing the complex was done using ChimeraX (55, 56) v1.6rc on relaxed models.

Statistics

Statistical analysis was performed with using PRISM9 (version 5.1) software. Statistical tests are indicated in the respective figure legend.

ACKNOWLEDGMENTS

We are extremely grateful to the patients from the HUG, who contributed lung tissue for this research project. We would like to express our gratitude to the surgery team of the thoracic surgery unit of the HUG. We thank the bioimaging platform of the CMU.

AUTHOR AFFILIATIONS

[1]Department of Microbiology and Molecular Medicine, Medical Faculty, University of Geneva, Geneva, Switzerland

[2]Bioimaging Core Facility, Medical Faculty, University of Geneva, Geneva, Switzerland
[3]Genomic Research Laboratory, Division of Infectious Diseases, Department of Medicine, University Hospitals and University of Geneva, Geneva, Switzerland
[4]Thoracic Surgery, Geneva University Hospitals, Geneva, Switzerland
[5]Geneva Center for inflammation research, Medical Faculty, University of Geneva, Geneva, Switzerland

PRESENT ADDRESS

Inês Boal-Carvalho, Department of Haematology, University College London Cancer Institute, London, United Kingdom

AUTHOR ORCIDs

Mirco Schmolke http://orcid.org/0000-0002-2491-3029

FUNDING

Funder	Grant(s)	Author(s)
Schweizerischer Nationalfonds zur Förderung der Wissenschaftlichen Forschung (SNF)	310030_212216, 310030_155949	Mirco Schmolke

AUTHOR CONTRIBUTIONS

Filo Silva, Formal analysis, Investigation, Methodology, Visualization | Inês Boal-Carvalho, Conceptualization, Formal analysis, Investigation | Nathalia Williams, Formal analysis, Investigation, Visualization | Mehdi Chabert, Investigation, Software, Visualization, Writing – original draft | Chengyue Niu, Investigation, Visualization | Dalila Hedhili, Investigation | Hélèna Choltus, Investigation | Nicolas Liaudet, Methodology, Software | Nadia Gaïa, Data curation, Formal analysis, Software | Wolfram Karenovics, Investigation, Resources | Patrice Francois, Formal analysis, Investigation, Methodology, Software, Writing – original draft | Mirco Schmolke, Conceptualization, Formal analysis, Funding acquisition, Investigation, Visualization, Writing – original draft, Writing – review and editing

ETHICS APPROVAL

Work with human patient material was approved by the internal review board under ref ID 2022-01942. All human donors of lung tissue for the generation of PCLS provided informed written consent. Patient samples were de-identified.

ADDITIONAL FILES

The following material is available online.

Supplemental Material

Fig. S1 (JVI00411-24-s0001.eps). Motif identification, alpha fold and peptides.
Supplemental figure legends (JVI00411-24-s0002.pdf). Legends for Fig. S1 to S6.
Fig. S2 (JVI00411-24-s0003.eps). Inverse pulldowns.
Fig. S3 (JVI00411-24-s0004.eps). Motif prevalence.
Fig. S4 (JVI00411-24-s0005.eps). Full-length pulldown.
Fig. S5 (JVI00411-24-s0006.eps). Representative confocal IF pictures PB1-F2 Cterm with NLRP3 domains.
Fig. S6 (JVI00411-24-s0007.eps). ISG mRNA induction after infection.
Scripts 1 to 4 (JVI00411-24-s0008.docx). Scripts for colocalization and motif extraction.
Table S1 (JVI00411-24-s0009.pdf). Donor information for PCLS.
Table S2 (JVI00411-24-s0010.pdf). Oligonucleotides.

REFERENCES

1. Oldstone MBA, Rosen H. 2014. Cytokine storm plays a direct role in the morbidity and mortality from influenza virus infection and is chemically treatable with a single sphingosine-1-phosphate agonist molecule. Curr Top Microbiol Immunol 378:129–147. https://doi.org/10.1007/978-3-319-05879-5_6
2. Kim KS, Jung H, Shin IK, Choi BR, Kim DH. 2015. Induction of Interleukin-1 beta (IL-1β) is a critical component of lung inflammation during influenza A (H1N1) virus infection. J Med Virol 87:1104–1112. https://doi.org/10.1002/jmv.24138
3. Kuriakose T, Kanneganti TD. 2017. Regulation and functions of NLRP3 inflammasome during influenza virus infection. Mol Immunol 86:56–64. https://doi.org/10.1016/j.molimm.2017.01.023
4. Zheng H, Fletcher D, Kozak W, Jiang M, Hofmann KJ, Conn CA, Soszynski D, Grabiec C, Trumbauer ME, Shaw A. 1995. Resistance to fever induction and impaired acute-phase response in interleukin-1β-deficient mice. Immunity 3:9–19. https://doi.org/10.1016/1074-7613(95)90154-x
5. Schmitz N, Kurrer M, Bachmann MF, Kopf M. 2005. Interleukin-1 is responsible for acute lung Immunopathology but increases survival of respiratory influenza virus infection. J Virol 79:6441–6448. https://doi.org/10.1128/JVI.79.10.6441-6448.2005
6. Lapuente D, Storcksdieck Genannt Bonsmann M, Maaske A, Stab V, Heinecke V, Watzstedt K, Heß R, Westendorf AM, Bayer W, Ehrhardt C, Tenbusch M. 2018. IL-1β as mucosal vaccine adjuvant: the specific induction of tissue-resident memory T cells improves the heterosubtypic immunity against influenza A viruses. Mucosal Immunol 11:1265–1278. https://doi.org/10.1038/s41385-018-0017-4
7. Zhang S, Sun F, Zhu J, Qi J, Wang W, Liu Z, Li W, Liu C, Liu X, Wang N, Song X, Zhang D, Qi D, Wang X. 2023. Phillyrin ameliorates influenza a virus-induced pulmonary inflammation by antagonizing CXCR2 and inhibiting NLRP3 inflammasome activation. Virol J 20:262. https://doi.org/10.1186/s12985-023-02219-4
8. Docherty CA, Fernando AJ, Rosli S, Lam M, Dolle RE, Navia MA, Farquhar R, La France D, Tate MD, Murphy CK, Rossi AG, Mansell A. 2023. A novel dual NLRP1 and NLRP3 inflammasome inhibitor for the treatment of inflammatory diseases. Clin Transl Immunol 12:e1455. https://doi.org/10.1002/cti2.1455
9. Tate MD, Ong JDH, Dowling JK, McAuley JL, Robertson AB, Latz E, Drummond GR, Cooper MA, Hertzog PJ, Mansell A. 2016. Reassessing the role of the NLRP3 inflammasome during pathogenic influenza A virus infection via temporal inhibition. Sci Rep 6:27912. https://doi.org/10.1038/srep27912
10. Fantuzzi G, Ku G, Harding MW, Livingston DJ, Sipe JD, Kuida K, Flavell RA, Dinarello CA. 1997. Response to local inflammation of IL-1 beta-converting enzyme- deficient mice. J Immunol 158:1818–1824. https://doi.org/10.4049/jimmunol.158.4.1818
11. Schmid-Burgk JL, Chauhan D, Schmidt T, Ebert TS, Reinhardt J, Endl E, Hornung V. 2016. A genome-wide CRISPR (clustered regularly interspaced short palindromic repeats) screen identifies NEK7 as an essential component of NLRP3 inflammasome activation. J Biol Chem 291:103–109. https://doi.org/10.1074/jbc.C115.700492
12. He Y, Zeng MY, Yang D, Motro B, Núñez G. 2016. NEK7 is an essential mediator of NLRP3 activation downstream of potassium efflux. Nature 530:354–357. https://doi.org/10.1038/nature16959
13. Sharif H, Wang L, Wang WL, Magupalli VG, Andreeva L, Qiao Q, Hauenstein AV, Wu Z, Núñez G, Mao Y, Wu H. 2019. Structural mechanism for NEK7-licensed activation of NLRP3 inflammasome. Nature 570:338–343. https://doi.org/10.1038/s41586-019-1295-z
14. Vajjhala PR, Mirams RE, Hill JM. 2012. Multiple binding sites on the pyrin domain of ASC protein allow self-association and interaction with NLRP3 protein. J Biol Chem 287:41732–41743. https://doi.org/10.1074/jbc.M112.381228
15. Oroz J, Barrera-Vilarmau S, Alfonso C, Rivas G, de Alba E. 2016. ASC pyrin domain self-associates and binds NLRP3 protein using equivalent binding interfaces. J Biol Chem 291:19487–19501. https://doi.org/10.1074/jbc.M116.741082
16. Proell M, Gerlic M, Mace PD, Reed JC, Riedl SJ. 2013. The CARD plays a critical role in ASC foci formation and inflammasome signalling. Biochem J 449:613–621. https://doi.org/10.1042/BJ20121198
17. Andrei C, Dazzi C, Lotti L, Torrisi MR, Chimini G, Rubartelli A. 1999. The secretory route of the leaderless protein interleukin 1β involves exocytosis of endolysosome-related vesicles. Mol Biol Cell 10:1463–1475. https://doi.org/10.1091/mbc.10.5.1463
18. Andrei C, Margiocco P, Poggi A, Lotti LV, Torrisi MR, Rubartelli A. 2004. Phospholipases C and A_2 control lysosome-mediated IL-1β secretion: implications for inflammatory processes. Proc Natl Acad Sci USA 101:9745–9750. https://doi.org/10.1073/pnas.0308558101
19. Bergsbaken T, Fink SL, Cookson BT. 2009. Pyroptosis: host cell death and inflammation. Nat Rev Microbiol 7:99–109. https://doi.org/10.1038/nrmicro2070
20. Boal-Carvalho I, Mazel-Sanchez B, Silva F, Garnier L, Yildiz S, Bonifacio JP, Niu C, Williams N, Francois P, Schwerk N, Schöning J, Carlens J, Viemann D, Hugues S, Schmolke M. 2020. Influenza A viruses limit NLRP3-NEK7-complex formation and pyroptosis in human macrophages. EMBO Rep 21:e50421. https://doi.org/10.15252/embr.202050421
21. Jumper J, Evans R, Pritzel A, Green T, Figurnov M, Ronneberger O, Tunyasuvunakool K, Bates R, Žídek A, Potapenko A, et al. 2021. Highly accurate protein structure prediction with AlphaFold. Nature 596:583–589. https://doi.org/10.1038/s41586-021-03819-2
22. Varadi M, Anyango S, Deshpande M, Nair S, Natassia C, Yordanova G, Yuan D, Stroe O, Wood G, Laydon A, et al. 2022. AlphaFold protein structure database: massively expanding the structural coverage of protein-sequence space with high-accuracy models. Nucleic Acids Res 50:D439–D444. https://doi.org/10.1093/nar/gkab1061
23. Gibbs JS, Malide D, Hornung F, Bennink JR, Yewdell JW. 2003. The influenza A virus PB1-F2 protein targets the inner mitochondrial membrane via a predicted basic amphipathic helix that disrupts mitochondrial function. J Virol 77:7214–7224. https://doi.org/10.1128/JVI.77.13.7214-7224.2003
24. Viana F, O'Kane CM, Schroeder GN. 2022. Precision-cut lung slices: a powerful *ex vivo* model to investigate respiratory infectious diseases. Mol Microbiol 117:578–588. https://doi.org/10.1111/mmi.14817
25. Cheung P-HH, Lee T-WT, Chan C-P, Jin D-Y. 2020. Influenza A virus PB1-F2 protein: an ambivalent innate immune modulator and virulence factor. J Leukoc Biol 107:763–771. https://doi.org/10.1002/JLB.4MR0320-206R
26. Chen W, Calvo PA, Malide D, Gibbs J, Schubert U, Bacik I, Basta S, O'Neill R, Schickli J, Palese P, Henklein P, Bennink JR, Yewdell JW. 2001. A novel influenza A virus mitochondrial protein that induces cell death. Nat Med 7:1306–1312. https://doi.org/10.1038/nm1201-1306
27. McAuley JL, Chipuk JE, Boyd KL, Van De Velde N, Green DR, McCullers JA. 2010. PB1-F2 proteins from H5N1 and 20th century pandemic influenza viruses cause immunopathology. PLoS Pathog 6:e1001014. https://doi.org/10.1371/journal.ppat.1001014
28. Solbak SMØ, Sharma A, Bruns K, Röder R, Mitzner D, Hahn F, Niebert R, Vedeler A, Henklein P, Henklein P, Schubert U, Wray V, Fossen T. 2013. Influenza A virus protein PB1-F2 from different strains shows distinct structural signatures. Biochim Biophys Acta 1834:568–582. https://doi.org/10.1016/j.bbapap.2012.11.009
29. Cheng Y-Y, Yang S-R, Wang Y-T, Lin Y-H, Chen C-J. 2017. Amino acid residues 68-71 contribute to influenza A virus PB1-F2 protein stability and functions. Front Microbiol 8:692. https://doi.org/10.3389/fmicb.2017.00692
30. Alymova IV, Samarasinghe A, Vogel P, Green AM, Weinlich R, McCullers JA. 2014. A novel cytotoxic sequence contributes to influenza A viral protein PB1-F2 pathogenicity and predisposition to secondary bacterial infection. J Virol 88:503–515. https://doi.org/10.1128/JVI.01373-13
31. Cheung P-HH, Lee T-WT, Kew C, Chen H, Yuen K-Y, Chan C-P, Jin D-Y. 2020. Virus subtype-specific suppression of MAVS aggregation and activation by PB1-F2 protein of influenza A (H7N9) virus. PLoS Pathog 16:e1008611. https://doi.org/10.1371/journal.ppat.1008611
32. Wang R, Zhu Y, Ren C, Yang S, Tian S, Chen H, Jin M, Zhou H. 2021. Influenza A virus protein PB1-F2 impairs innate immunity by inducing mitophagy. Autophagy 17:496–511. https://doi.org/10.1080/15548627.2020.1725375
33. Mettier J, Marc D, Sedano L, Da Costa B, Chevalier C, Le Goffic R. 2021. Study of the host specificity of PB1-F2-associated virulence. Virulence 12:1647–1660. https://doi.org/10.1080/21505594.2021.1933848

34. Alymova IV, Green AM, van de Velde N, McAuley JL, Boyd KL, Ghoneim HE, McCullers JA. 2011. Immunopathogenic and antibacterial effects of H3N2 influenza A virus PB1-F2 map to amino acid residues 62, 75, 79, and 82. J Virol 85:12324–12333. https://doi.org/10.1128/JVI.05872-11
35. Chung W-C, Kang H-R, Yoon H, Kang S-J, Ting JP-Y, Song MJ. 2015. Influenza A virus NS1 protein inhibits the NLRP3 inflammasome. PLoS One 10:e0126456. https://doi.org/10.1371/journal.pone.0126456
36. Chevalier C, Leymarie O, Sedano L, Da Costa B, Richard C-A, Maisonnasse P, Réfregiers M, Jamme F, Le Goffic R. 2021. PB1-F2 amyloid-like fibers correlate with proinflammatory signaling and respiratory distress in influenza-infected mice. J Biol Chem 297:100885. https://doi.org/10.1016/j.jbc.2021.100885
37. Cheung P-HH, Ye Z-W, Lee T-WT, Chen H, Chan C-P, Jin D-Y. 2020. PB1-F2 protein of highly pathogenic influenza A (H7N9) virus selectively suppresses RNA-induced NLRP3 inflammasome activation through inhibition of MAVS-NLRP3 interaction. J Leukoc Biol 108:1655–1663. https://doi.org/10.1002/JLB.4AB0420-694R
38. Kalantar K, Farzaneh Z, Gholijani N, Hosseini SY, Bani Hasan E. 2020. Pro-inflammatory effects of influenza type A virus PB1-F2 protein-derived peptide in lipopolysaccharide-treated macrophages. Iran J Allergy Asthma Immunol 19:74–82. https://doi.org/10.18502/ijaai.v19i(s1.r1).2863
39. Pinar A, Dowling JK, Bitto NJ, Robertson AAB, Latz E, Stewart CR, Drummond GR, Cooper MA, McAuley JL, Tate MD, Mansell A. 2017. PB1-F2 peptide derived from avian influenza A virus H7N9 induces inflammation via activation of the NLRP3 inflammasome. J Biol Chem 292:826–836. https://doi.org/10.1074/jbc.M116.756379
40. Zell R, Krumbholz A, Eitner A, Krieg R, Halbhuber KJ, Wutzler P. 2007. Prevalence of PB1-F2 of influenza A viruses. J Gen Virol 88:536–546. https://doi.org/10.1099/vir.0.82378-0
41. Hai R, Schmolke M, Varga ZT, Manicassamy B, Wang TT, Belser JA, Pearce MB, García-Sastre A, Tumpey TM, Palese P. 2010. PB1-F2 expression by the 2009 pandemic H1N1 influenza virus has minimal impact on virulence in animal models. J Virol 84:4442–4450. https://doi.org/10.1128/JVI.02717-09
42. Xiao L, Magupalli VG, Wu H. 2023. Cryo-EM structures of the active NLRP3 inflammasome disc. Nature 613:595–600. https://doi.org/10.1038/s41586-022-05570-8
43. Andreeva L, David L, Rawson S, Shen C, Pasricha T, Pelegrin P, Wu H. 2021. NLRP3 cages revealed by full-length mouse NLRP3 structure control pathway activation. Cell 184:6299–6312. https://doi.org/10.1016/j.cell.2021.11.011
44. Hochheiser IV, Pilsl M, Hagelueken G, Moecking J, Marleaux M, Brinkschulte R, Latz E, Engel C, Geyer M. 2022. Structure of the NLRP3 decamer bound to the cytokine release inhibitor CRID3. Nature 604:184–189. https://doi.org/10.1038/s41586-022-04467-w
45. Ohto U, Kamitsukasa Y, Ishida H, Zhang Z, Murakami K, Hirama C, Maekawa S, Shimizu T. 2022. Structural basis for the oligomerization-mediated regulation of NLRP3 inflammasome activation. Proc Natl Acad Sci USA 119:e2121353119. https://doi.org/10.1073/pnas.2121353119
46. Mazel-Sanchez B, Boal-Carvalho I, Silva F, Dijkman R, Schmolke M. 2018. H5N1 influenza A virus PB1-F2 relieves HAX-1-mediated restriction of avian virus polymerase PA in human lung cells. J Virol 92:e00425-18. https://doi.org/10.1128/JVI.00425-18
47. Schmolke M, Manicassamy B, Pena L, Sutton T, Hai R, Varga ZT, Hale BG, Steel J, Pérez DR, García-Sastre A. 2011. Differential contribution of PB1-F2 to the virulence of highly pathogenic H5N1 influenza A virus in mammalian and avian species. PLoS Pathog 7:e1002186. https://doi.org/10.1371/journal.ppat.1002186
48. Bankhead P, Loughrey MB, Fernández JA, Dombrowski Y, McArt DG, Dunne PD, McQuaid S, Gray RT, Murray LJ, Coleman HG, James JA, Salto-Tellez M, Hamilton PW. 2017. QuPath: open source software for digital pathology image analysis. Sci Rep 7:16878. https://doi.org/10.1038/s41598-017-17204-5
49. Pachitariu M, Stringer C. 2022. Cellpose 2.0: how to train your own model. Nat Methods 19:1634–1641. https://doi.org/10.1038/s41592-022-01663-4
50. Manders EMM, Verbeek FJ, Aten JA. 1993. Measurement of co-localization of objects in dual-colour confocal images. J Microsc 169:375–382. https://doi.org/10.1111/j.1365-2818.1993.tb03313.x
51. Anchisi S, Gonçalves AR, Mazel-Sanchez B, Cordey S, Schmolke M. 2018. Influenza A virus genetic tools: from clinical sample to molecular clone. Methods Mol Biol 1836:33–58. https://doi.org/10.1007/978-1-4939-8678-1_3
52. Sievers F, Wilm A, Dineen D, Gibson TJ, Karplus K, Li W, Lopez R, McWilliam H, Remmert M, Söding J, Thompson JD, Higgins DG. 2011. Fast, scalable generation of high-quality protein multiple sequence alignments using Clustal Omega. Mol Syst Biol 7:539. https://doi.org/10.1038/msb.2011.75
53. Goujon M, McWilliam H, Li W, Valentin F, Squizzato S, Paern J, Lopez R. 2010. A new bioinformatics analysis tools framework at EMBL-EBI. Nucleic Acids Res 38:W695–W699. https://doi.org/10.1093/nar/gkq313
54. Mirdita M, Schütze K, Moriwaki Y, Heo L, Ovchinnikov S, Steinegger M. 2022. ColabFold: making protein folding accessible to all. Nat Methods 19:679–682. https://doi.org/10.1038/s41592-022-01488-1
55. Pettersen EF, Goddard TD, Huang CC, Meng EC, Couch GS, Croll TI, Morris JH, Ferrin TE. 2021. UCSF ChimeraX: structure visualization for researchers, educators, and developers. Protein Sci 30:70–82. https://doi.org/10.1002/pro.3943
56. Goddard TD, Huang CC, Meng EC, Pettersen EF, Couch GS, Morris JH, Ferrin TE. 2018. UCSF ChimeraX: meeting modern challenges in visualization and analysis. Protein Sci 27:14–25. https://doi.org/10.1002/pro.3235